Computational Analysis of Martensitic Thin Films using Subdivision Surfaces

Patrick W. Dondl, Ching-Ping Shen and Kaushik Bhattacharya

June 28, 2006

Abstract

This paper studies numerically the deformation of thin films made of materials undergoing martensitic phase transformations by using subdivision surfaces. These thin films have received interest as potential microactuators, and specifically a tent-like configuration has recently been proposed. The study of such configurations requires adequate resolution of inhomogeneous in-plane stretch, out-of-plane deformation and transition regions across which the deformation gradient changes sharply. This paper demonstrates that subdivision surfaces provide an attractive tool in the numerical study of such configurations, and also provides insights into the tent-like deformations.

1 Introduction

Thin films of shape-memory alloys have received attention as potential microactuators since the recognition that they possess the largest work per unit volume among possible actuator systems [7]. This is because the martensitic phase transformation, a solid-to-solid phase transformation responsible for the shape-memory effect, provides a direct link between the macroscopic deformation and microscopic changes in the crystalline unit cell. This advantage is maximized by using single crystal thin films where the geometry of the structure is carefully chosen to be consistent with the inherent crystallography of the material. This, however, requires careful analysis of the deformation and this in turn requires a numerical method that is capable of resolving inhomogeneous in-plane stretch, out-of-plane deformation and transition regions across which the deformation gradient changes sharply. Such an analysis is the goal of the paper.

The martensitic phase transformation is a diffusionless process where, at a certain temperature θ_c, the preferred crystallographic configuration of the material changes. Typically, the high-temperature phase, the austenite, has greater symmetry than the low-temperature phase, the martensite, and therefore the martensite has a number of symmetry-related variants. Consequently the energy density of the material has a multi-well structure, with each well associated with a different phase/variant. The different phases may co-exist in a configuration, and one also has an interfacial energy which is often modeled as a quadratic penalization of the strain gradient.

This raises the numerical difficulty, common to many other structural and materials problems, of accurately evaluating energies which depend on the first as well as second derivatives of the deformation. Numerical evaluation of such energies requires a discretization which is continuous in the deformation as well as in its first derivative. Consequently one can not use simple linear elements, and higher order polynomials bring their own problems. Cirak and Ortiz [4] addressed this by adapting sub-division surfaces, which were introduced and widely used in computer graphics (see for example, [10]), as elements to study finite deformation of thin-shells. We further develop this approach, and demonstrate how subdivision surfaces can be used for the study of martensitic thin films.

Our starting point is the theory of martensitic thin films proposed by Bhattacharya and James [2]. We use our computational method to explore in detail a tent-like deformation that has potential application as an actuator. The idea is to deposit a single crystal thin film of a martensitic material on a (silicon) substrate in such a manner that it is approximately lattice-matched to the austenite. Then, a small square region of the film is released by back-etching to give a free-standing membrane which is bonded on all sides. The free-standing region is in the austenite state when hot but transforms to the martensite on cooling. Further, if the crystallography of the material satisfies some special conditions, and if the orientation of the released region matches specific crystallographic directions of the material, then the films pops up like a tent in the martensitic state. Therefore we have a configuration that switches between a flat and a tent-like shape when subjected to temperature cycling.

A detailed understanding of the exact nature of the deformation is the first motivation of our study. While the overall shape and structure conforms to the simplified analysis of Bhattacharya and James [2], we find an unexpected breaking of the symmetry at the tip. Studying the effects of misalignment is the second aim of our work, since it is difficult in practice to align the released region exactly with the crystallography of the material. We find that the overall structure remains stable for small deviations but it begins to deviate substantially beyond 10 degrees of misalignment. Finally, since the released area may not be a square, we study a rectangular region as an example.

Belik and Luskin [1] also studied tent-like deformation using a finite element method. However, their model of interfacial energy replaces higher order derivatives with a term that lives on the element edges. Consequently, their energy depends critically on the triangulation and they arranged their triangulation in a way such that the expected phase/variant boundaries lie on such edges. Unfortunately such an approach requires an accurate a priori knowledge of the phase/variant boundaries and this is not possible in the situations like those describe above.

The article is organized as follows. In Section 2, the continuum model and the relevant energy terms are introduced. The details of the finite element simulation are described in Section 3, followed by a short review in Section 4 of the subdivision surface method proposed in [5]. Section 5 contains the simulation results. Section 6 verifies our computational results further with some analytical calculations. Some discussion of these results and an outlook to further improvements on this method are given in Section 7.
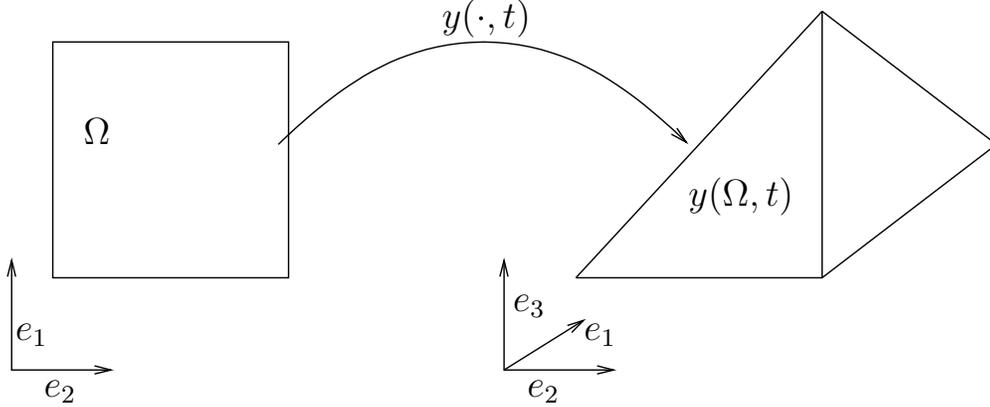
Figure 1: Deformation of a reference configuration Ω at a certain time t.

2   The model of thin films

Consider a thin film occupying a flat reference configuration $\Omega \subset \mathbb{R}^2$ and undergoing a time-dependent deformation $y \colon \Omega \times \mathbb{R}^+ \to \mathbb{R}^3$ as depicted in Figure 1. We assume that $y(x,t)$ is injective and orientation preserving in the plane for all times. Furthermore, assume that $y(x,t)$ is sufficiently smooth to compute the deformation gradient $F(t) = \nabla y(t)$ and the second derivatives almost everywhere.

The dynamics of the film are governed by an energy consisting of the kinetic energy E_{kin}, a multi-well strain energy E_{strain}, and the interfacial or exchange energy $E_{\text{interfacial}}$, modeled using a higher (or strain) gradient. After suitable non-dimensionalization, these energies can be written as follows.

Kinetic energy.   The kinetic energy is given by

$$E_{\text{kin}} = \int_\Omega \frac{1}{2} \left| y_t \right|^2 \, \mathrm{d}x.$$

Strain energy.   The strain energy of the crystal is given as the integral of the strain energy density W,

$$E_{\text{strain}} = \int_\Omega W(F(x)) \, \mathrm{d}x.$$

To model the phase transition of the shape-memory material, one can use a strain energy density with multiple minima at the preferred positions in the strain space. Frame indifference requires the energy to be a function of the right Cauchy-Green strain tensor $C = F^{\mathrm{T}} F$ alone. In our case, we consider a cubic-tetragonal phase transition and thus assume W to be of the form

$$\begin{aligned} W(F) = W(C_{ij}) \;\; = \;\; & a \cdot \left(C_{11} + C_{22} - \xi^2 \right)^2 + \\ & b \cdot \Phi(C_{11} - C_{22}) \left((C_{11} - C_{22})^2 - \xi^4 \right)^2 + c \cdot C_{12}^2 \end{aligned} \tag{1}$$
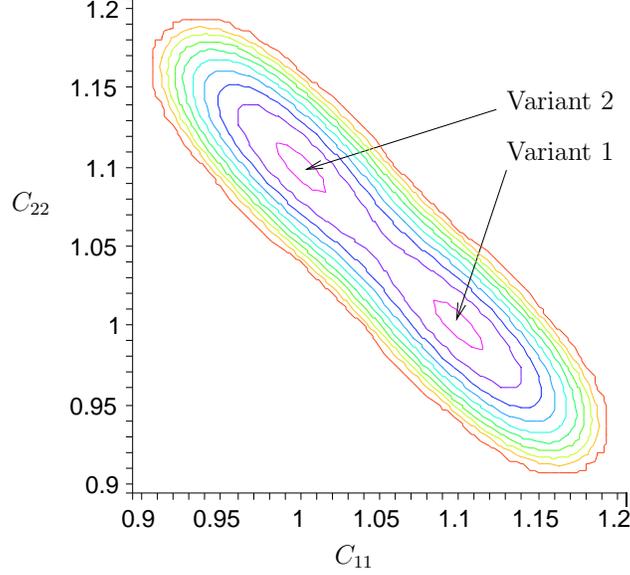
with positive coefficients a, b, and c.

Figure 2: Contour plot of the energy landscape in the C_{11}-C_{22} plane.

The function Φ augments the energy barrier in the nonconvex term of the strain energy and is given by

$$\Phi(q) = 1 + \eta \cdot e^{\frac{-q^2}{\kappa \xi^2}}, \tag{2}$$

with two parameters η and κ. The energy density has its minima on the set

$$O(2,3)U_1 \cup O(2,3)U_2$$

where

$$U_1 = \begin{pmatrix} \sqrt{1+\xi^2} & 0 \\ 0 & 1 \end{pmatrix} \text{ and } U_2 = \begin{pmatrix} 1 & 0 \\ 0 & \sqrt{1+\xi^2} \end{pmatrix}.$$

are the transformation stretches of the two variants of martensite, and $O(2,3) = \{A \in \text{Mat}(3,2) : A^{\mathrm{T}}A = \text{Id}_{2\times2}\}$. Notice that one variant represents stretching in the x_1-direction while the other represents stretching in the x_2-direction. The contour plot of the energy is shown in Figure 2.

For later use, we also consider the following. We will be interested in situations where the crystallographic axes do not coincide with the coordinate axis. In such sitatuions, we will take the energy density to be of the form

$$W(R^{\mathrm{T}}C(x)R) \tag{3}$$

where $R \in SO(2)$ is the rotation matrix that takes the crystallographic axes to the coordinate axes.

Interfacial Energy   The interfacial energy penalizes changes in the gradient and introduces an inherent length scale in the system. The interfacial energy used is given by

$$E_{\text{interfacial}} = \int_\Omega \frac{1}{2} |\triangle y|^2 \, \mathrm{d}x. \tag{4}$$

4

Two comments are in order. First, this energy is apparently different from the commonly used form

$$\int_\Omega \frac{1}{2} \left| \nabla^2 y \right|^2 \, \mathrm{d}x$$

where $\nabla^2 y$ denotes the third order tensor of second derivatives of y. However, these two terms differ only by a null-Lagrangian (i.e., terms which can be written exclusively in terms of boundary values). Therefore both energies yield the same governing equation. Further, since we use only the clamped boundary condition, the boundary term is in fact zero so that both forms agree. Second, observe that this energy also penalizes bending. In fact, $|\triangle y_3|^2 = |y_{3,11} + y_{3,22}|^2$ is the energy of bending for small deflections. However, in this paper, we shall think of this energy as arising due to interfacial energy.

Using these energies, we derive the non-dimensionalized dynamic equations using the principle of stationary action:

$$\delta S = 0$$

where S is the action integral given by

$$S = \int_{t_0}^{t_1} \mathscr{L} \, \mathrm{d}t.$$

with Lagrangian

$$\mathscr{L} = E_{\mathrm{kin}} - E_{\mathrm{strain}} - E_{\mathrm{interfacial}}.$$

Substituting the expressions for the energy into the action integral yields

$$
\begin{aligned}
0 &= \delta S \\
&= \delta \int_{t_0}^{t_1} \int_\Omega \frac{1}{2} |y_t(x,t)|^2 - W(F(x,t)) - \frac{1}{2} |\triangle y(x,t)|^2 \, \mathrm{d}x \, \mathrm{d}t \\
&= \int_{t_0}^{t_1} \int_\Omega y_{tt}(x,t) \cdot \delta y(x,t) - \frac{\partial W(x,t)}{\partial F} \cdot \nabla \delta y(x,t) \, \mathrm{d}x \, \mathrm{d}t \\
&\quad - \int_{t_0}^{t_1} \int_\Omega y_{tt}(x,t) \triangle y(x,t) \cdot \triangle \delta y(x,t) \, \mathrm{d}x \, \mathrm{d}t \,.
\end{aligned}
\tag{5}
$$

Since none of the energy terms are explicitly time-dependent, and the variations of y can be chosen arbitrarily in time, equation (5) is equivalent to

$$0 = \int_\Omega y_{tt}(x,t) \cdot \delta y(x) - \sigma \cdot \nabla \delta y(x) - \triangle y(x,t) \cdot \triangle \delta y(x) \, \mathrm{d}x. \tag{6}$$

where

$$\sigma(x,t) = \frac{\partial W(x,t)}{\partial F}$$

is the Piola-Kirchhoff stress.

In this paper, we are interested in the equilibrium states. To obtain them from the dynamic equations above, we introduce dissipation in the system.
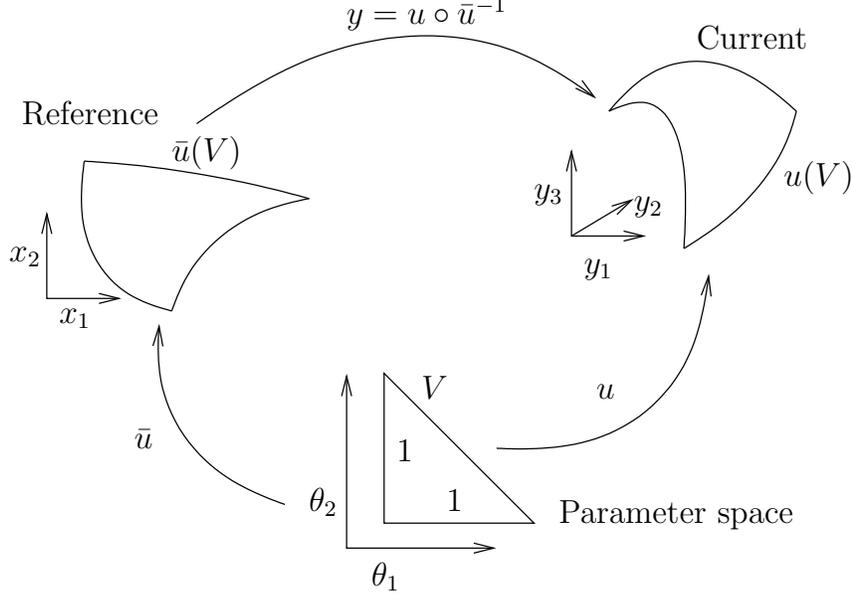
Figure 3: Mapping of unit triangle to deformed and undeformed configuration.

Dissipation We introduce linear dissipation by augmenting (6) with the following term on the right hand side:

$$- \int_\Omega \beta F_t \cdot \nabla \delta y(x) \, \mathrm{d}x.$$

It is easy to show that

$$\frac{d}{dt} \left(E_{\mathrm{kin}} + E_{\mathrm{strain}} + E_{\mathrm{interfacial}} \right) = \beta \int_\Omega |F_t|^2 \, \mathrm{d}x.$$

The viscosity parameter β is of the order of 0.1, but it is increased when the simulation gets closer to the equilibrium configuration, in order to accelerate the loss of energy.

In summary, our model of thin films is given in weak form by

$$0 = \int_\Omega y_{tt}(x,t) \cdot \delta y(x) - \sigma \cdot \nabla \delta y(x) - \triangle y(x,t) \cdot \triangle \delta y(x) - \beta F_t \cdot \nabla \delta y(x) \, \mathrm{d}x \qquad (7)$$

for all $\delta y(x) : \Omega \to \mathbb{R}^3$ consistent with boundary conditions at each time t.

3 Numerical method

We seek to use the finite-element method to solve (7). This however requires care since this equation contains second derivatives of the displacement. In particular, our basis should have continuous first derivatives and we can not use the standard piecewise affine basis. We use subdivision surfaces following [4]. A discussion of the details is deferred till Section 4 after we describe the formulation.

We describe the reference and deformed configuration using a parametrization as shown in Figure 3. In other words, consider a smooth local one-to-one mapping from a set $V \subset \mathbb{R}^2$

$$\bar{u}: V \rightarrow \Omega,$$
$$\bar{u}: \theta \mapsto x = \bar{u}(\theta),$$

which will later be induced by a triangulation of Ω, and a mapping

$$u: V \times \mathbb{R}^+ \rightarrow \mathbb{R}^3,$$
$$u: (\theta, t) \mapsto y = u(\theta, t),$$

such that

$$y(x, t) = (u(\cdot, t) \circ \bar{u}^{-1}(\cdot))(x).$$

It follows that $F = \nabla y = \nabla u \cdot (\nabla \bar{u})^{-1}$. The second derivatives of y can be computed in a similar fashion by noting that

$$0 = \frac{\partial}{\partial x_i} \text{Id} = \frac{\partial}{\partial x_i} \nabla \bar{u} \nabla \bar{u}^{-1} = \nabla \bar{u}_{x_i} \nabla \bar{u}^{-1} + \nabla \bar{u} \nabla \bar{u}_{x_i}^{-1}$$

and using the chain rule. Further, the variation in y is related to the variation in u by

$$\delta y(x) = \delta u \circ \bar{u}^{-1}.$$

In the following we often continue to write $\triangle y$ and $\triangle \delta y$ since the full expression using u and $\bar{u}$ are somewhat lengthy, but assume that they are written in terms of u and $\bar{u}$.

Now, assuming we have a non-overlapping set $\{V_q\}_{q=1}^m$ such that we have mappings u and $\bar{u}$ as above on all V_q and

$$\bigcup_{q=1}^m \bar{u}(V_q) = \Omega,$$

equation (7) yields

$$
\begin{aligned}
0 = \sum_{q=1}^m \Bigg[& \int_{\bar{u}(V_q)} (u_{tt}(\cdot, t) \circ (\bar{u}(\cdot))^{-1})(x) \cdot (\delta u(\cdot) \circ (\bar{u}(\cdot))^{-1})(x) \, dx \\
& - \int_{\bar{u}(V_q)} \sigma(\nabla u \cdot (\nabla \bar{u})^{-1}) \cdot \nabla \delta u \cdot (\nabla \bar{u})^{-1} \, dx \\
& - \int_{\bar{u}(V_q)} \triangle y \cdot \triangle \delta y \, dx \\
& - \int_{\bar{u}(V_q)} \beta \nabla u_t \cdot (\nabla \bar{u})^{-1} \cdot \nabla \delta u \cdot (\nabla \bar{u})^{-1} \, dx \Bigg],
\end{aligned}
$$

where all the functions u and $\bar{u}$ and their derivatives are evaluated at $\bar{u}^{-1}(x)$, as it is explicitly written in the first term. Now one can pull the integration back onto the parameter space

so that one has

$$
\begin{aligned}
0 \;=\; \sum_{q=1}^{m} \Bigg[\;\; & \int_{V_q} u_{tt} \cdot \delta u \, |\nabla \bar{u}| \mathrm{d}\theta \\
& - \int_{V_q} \sigma(\nabla u \cdot (\nabla \bar{u})^{-1}) \cdot \nabla \delta u \cdot (\nabla \bar{u})^{-1} \, |\nabla \bar{u}| \mathrm{d}\theta \\
& - \int_{V_q} \triangle y \cdot \triangle \delta y \, |\nabla \bar{u}| \mathrm{d}\theta \\
& - \int_{V_q} \beta \nabla u_t \cdot (\nabla \bar{u})^{-1} \cdot \nabla \delta u \cdot (\nabla \bar{u})^{-1} \, |\nabla \bar{u}| \mathrm{d}\theta \Bigg].
\end{aligned} \tag{8}
$$

We discretize $u, \bar{u}$ using the Loop subdivision surface basis functions $\{\varphi_i\}_{i=1}^{n}$ so that,

$$
\bar{u}(\theta) = \sum_{i=1}^{n} \bar{u}_i \varphi_i(\theta)
$$

and

$$
u(\theta, t) = \sum_{i=1}^{n} u_i(t) \varphi_i(\theta).
$$

with coefficients $u_i, \bar{u}_i$. With this discretization, we follow the usual finite element approach and enforce equation (8) for the test function δu in the span of $\{\varphi_j\}_{j=1}^{n}$. In our formulation, we treat the $\bar{u}_i$ associated with the reference configuration as fixed coefficients and the the u_i associated with the deformed configurations as variables which we solve for. This yields an equation of the form

$$
M\ddot{\mathbf{u}} = \mathbf{f}(\mathbf{u}, \dot{\mathbf{u}})
$$

with the mass matrix $M_{ij} = \sum_{q=1}^{m} \int_{V_q} \varphi_i \varphi_j \, |\nabla \bar{u}| \mathrm{d}\theta$. We compute all integrals using a simple one point approximation. We then lump the mass matrix in a row-sum manner and advance the remaining second order ordinary differential equation in time using a second order accurate explicit Newmark scheme.

4   Loop Subdivision Basis Functions

In order to provide a meaningful discretization of the continuous model in equation (7), we have already noted that the approximating functions need to be in H^2. A continuously differentiable discretization will provide such a setting.

We begin in one space dimension. Consider the discretization[1] shown in Figure 4. A simple linear finite element basis function associated with node 0 is shown as a dashed line. It is continuous but not continuously differentiable. Therefore, we would like to replace it with a C^1 (or smoother) basis function, as shown by the solid line while retaining two properties: first it has to have finite support and second it has to have one degree of freedom centered at the node. A cubic B-spline has exactly these properties, and the support is

---

[1]The discretization is shown to be regular but that is not necessary.
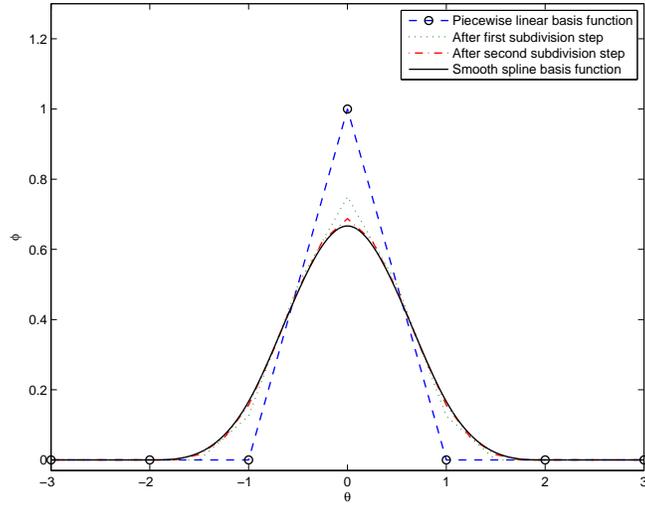
Figure 4: The piecewise linear basis function and the smooth spline basis function that it gets replaced with. Also shown are the first two steps of subdivision. Note that they are still polygonal lines, but converge to the smooth spline. The nodes are on every integer parameter value.
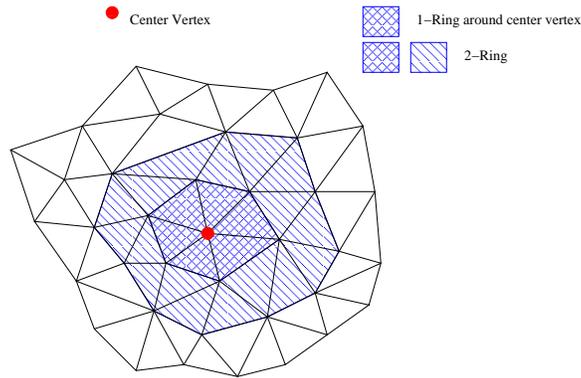

Figure 5: A triangulation with the support of the basis functions.

confined to four adjoining 'elements' centered around the middle node. In other words, we replace the dashed polygonal curve with the solid approximating spline curve using the same nodes.

To be precise, consider the two-dimensional polygonal curve connecting the n points $x_i^0 = (\theta^i, \phi^i)$. We can generate an approximating spline as follows (see for example, [10]). Generate a new set of $2n - 1$ points by subdivision:

$$x_{2i}^1 = \frac{1}{2}(x_i^0 + x_{i+1}^0)$$

and

$$x_{2i-1}^1 = \frac{1}{8}(x_{i-1}^0 + 6x_i^0 + x_{i+1}^0)$$

and connect them with a polygonal curve. The is shown in Figure 4. Repeating this process leads, in the limit, to a C^2 cubic spline curve. The linearity of the process ensures that the limiting curve can be written as a linear combination of basis functions with the original vertex positions as weights. Starting with the polygonal curve generated by the linear basis functions gives us a new basis function with the properties described above. This algorithm has to be modified for boundary nodes, but this is easily accomplished in one dimension.

We now extend this idea to two space dimensions. We start with a given triangulation as shown in Figure 5. As in one dimension, we seek to replace the piecewise linear basis functions with a C^1 basis function that is compactly supported and has one degree of freedom. The Loop subdivision basis functions [8] do so by replacing the polyhedral surface generated by the linear basis function with a C^1 surface. The basic idea is the quadrisection of triangles with a particular choice of weights for the new nodes. We refer the reader to Zorin and Schröder [10] for details. In our finite element context, the support of the chosen subdivision basis functions is the 2-ring of triangles around a given vertex , as shown in Figure 5. The particular basis functions depend on the topology (connectivity) of the triangulation.

Care has to be taken in fixing the boundary conditions, because of the extended support of the basis functions. One can either change the subdivision rules near the boundary to prescribe position and normal vectors to the surface at the boundary [3] or add a layer of "ghost" vertices around the domain as suggested in [5], which is the approach chosen here.

Our simulation uses the routine described in [9] to efficiently evaluate the basis functions for a given triangle patch.

In order to achieve the setting in Section 3, we start with a triangulation of the computational domain. The mapping $\bar{u}$ uses the vertex positions of that triangulation as coefficients. The deformed configuration then has variable coefficients in $\mathbb{R}^3$, which comprise the degrees of freedom in our computation.

5   Simulations

In this section we present the results of various numerical experiments motivated by the tent-like deformations described in the introduction. All simulations use the energy parameters

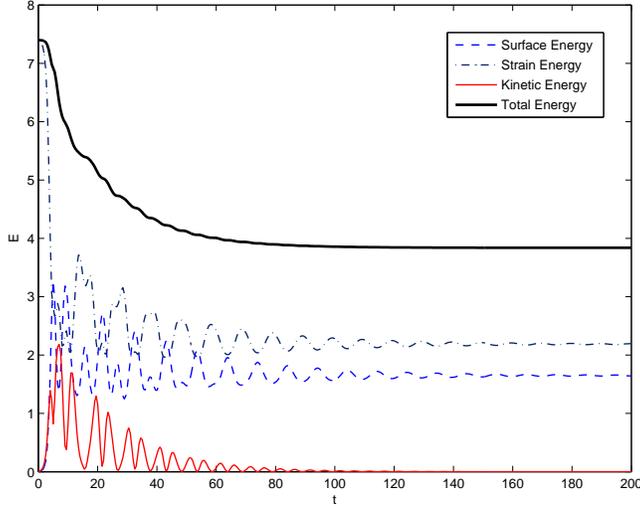$$a = 5.0, \quad b = 5.0, \quad c = 5.0, \quad \xi = 0.1, \quad \eta = 3.0, \quad \kappa = 1.0$$

Figure 6: Time dependency of the energy in the system

unless otherwise noted. In figures displaying the surfaces, the color indicates which energy well can be attributed to the respective position. All simulations use clamped boundary conditions, i.e.

$$y = \begin{pmatrix} x_1 \\ x_2 \\ 0 \end{pmatrix}, \quad (\nabla y)n = \begin{pmatrix} n_1 \\ n_2 \\ 0 \end{pmatrix} \qquad \text{on } \partial\Omega.$$

We start the simulations with an initial condition corresponding to a flat surface subjected to a small push in the vertical dimension, and wait till it bounces around and evolves into a tent-shaped structures. A typical plot of how the various energies involved behave over time is shown in Figure 6.

5.1 Regular Tent

Figures 7 and 8 show the shape and the details of the fully relaxed tent formed on a domain of size 50×50 domain non-dimensionalized units calculated using 16384 elements. Figure 7 shows a nice pyramidal shape with almost flat surfaces and rounded edges. Regions with deformation gradient close to the first well are colored blue, those close to the second are colored orange and the rest grey. The different variants are also labeled in Figure 7. Clearly the flat faces correspond to almost constant deformation gradient close to the wells. This is confirmed in Figure 8(a) which shows that the strain energy is concentrated at the boundary, ridges and tip. This is also consistent with the fact that $C_{11} + C_{22}$, $C_{11} - C_{22}$ and C_{12} stay close to the values at the bottoms of the energy well except in these regions.

It is clear from Figures 8(b)-8(d) that the deformation is quite complex involving the various components of the Cauchy-Green tensor. In particular, the deformation can *not* be described as a simple out-of-plan deformation (anti-plane shear) since this would force the Cauchy-Green tensor to be of the form

$$C = \begin{pmatrix} 1 + \alpha^2 & \alpha\beta \\ \alpha\beta & 1 + \beta^2 \end{pmatrix}.$$
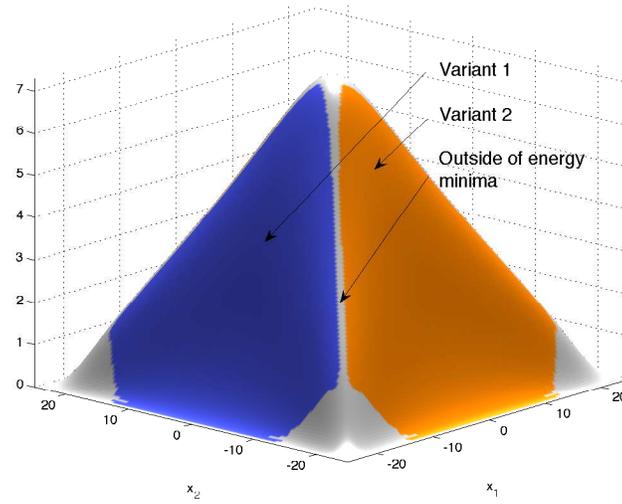
11

Figure 7: Shape of the fully relaxed regular tent. The numbering of the variants corresponds to Figure 2.
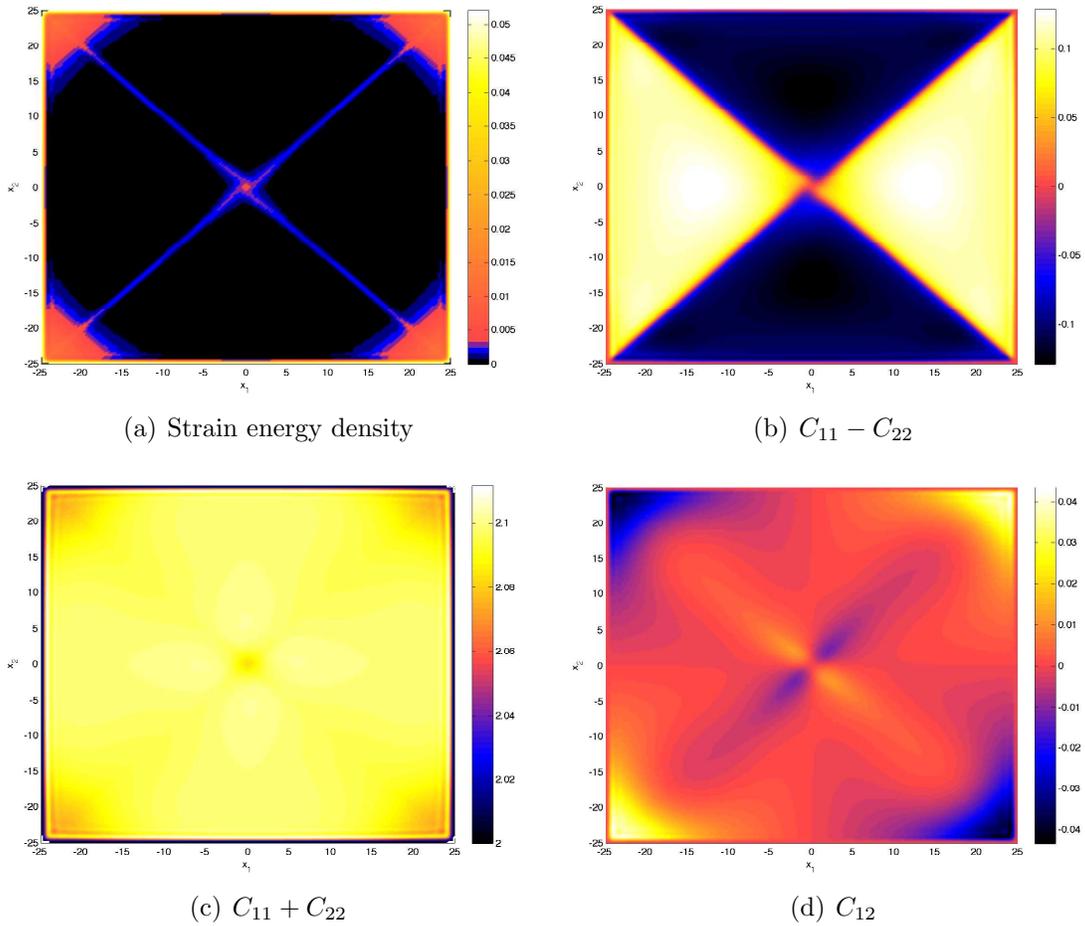

(a) Strain energy density

(b) $C_{11} - C_{22}$

(c) $C_{11} + C_{22}$

(d) C_{12}

Figure 8: Energy and strain variables of the regular tent.

Table 1: Comparison of base meshes of different resolution.

Number of Elements	256	1024	4096	16384
Absolute L^2 norm of surface height	30.0	35.1	37.3	38.1
L^2 norm of difference to next higher resolution	3.6	2.7	0.7	
Interfacial Energy	3.8	4.7	5.2	5.6
Strain Energy	28.4	15.1	8.6	5.4

It is also evident from Figures 8(b)-8(d) that the $C_{11} - C_{22}$ component of the Cauchy-Green tensor transitions from ξ^2 to $-\xi^2$ across the ridges whereas the $C_{11} + C_{22}$ and C_{12} components remain essentially uniform. In other words, In other words, the Cauchy-Green tensor effectively traverses the energy surface along the straight line as it transitions from one well to another along a ridge. This is not surprising given that the energy grows quickly (quadratically) in the convex directions, $C_{11} + C_{22}$ and C_{12}. We shall elaborate on this with some analytic considerations in Section 6.

Figure 8 also reveals that the computed tent is not exactly symmetric despite the fact the energy and geometry are. Instead, the tip where the four ridges meet appears to split into two creating a narrow strip of one contiguous variant. This asymmetry was observed in a simulation with a carefully constructed symmetric mesh and a symmetric initial condition. We also find that the mirror image of the solution shown in Figure 8 is equally stable. The tip of this steady state solution shows features similar to the tents with a slightly rotated strain energy density like in Section 5.4. However, a symmetric initial condition generated by symmetrizing this solution—in order to create a symmetric initial condition with very low energy—leads to a relaxed state that is symmetric. This symmetric state has slightly lower total energy than the asymmetrical one (11.01488 non-dimensionalized units, versus 11.01512 for the asymmetric tent).

We consider this breaking of symmetry real and not an artifact of numerical discretization, and believe that it constitutes a local minimum of the energy that has a significant domain of attraction.

Finally observe from Figure 8(a) that the energy density is highest near the boundary, especially at the corners, and significantly higher that that at the ridges and the tip. Our clamped boundary conditions force the deformation gradient to be identity and thus $C_{11} + C_{22}$ to take the value 2 at the corners (as also seen in Figure 8(c)). This value is different from the value $C_{11} + C_{22} = 2 + \xi^2$ at the bottom of the wells and the energy grows quadratically in this direction.

5.2   Convergence

A comparison of the tents formed in a region of size 50 by 50 (nondimensionalized units) with four different base meshes consisting of 256, 1025, 4096 and 16384 triangles is shown in Figure 9. Various quantitative details including L^2 norm of the height and energies are given in Table 5.2. We conclude that the 4096 element mesh provides a sufficient resolution for the following simulations and requires only a moderate amount of time to fully relax.
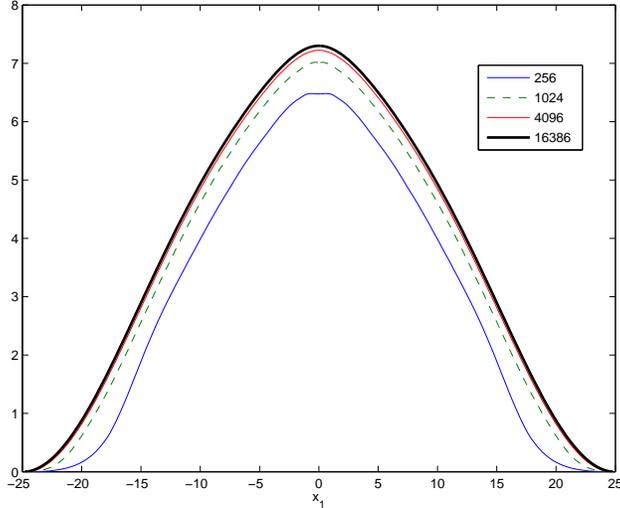
Figure 9: Cross section at $x_2 = 0$ of tents formed with different numbers of elements in the base mesh.

Table 2: Average energy density comparison for different domain sizes

Domain size	12×12	25×25	50×50
Interfacial energy per domain area	$1.4 \cdot 10^{-2}$	$5.1 \cdot 10^{-3}$	$2.1 \cdot 10^{-3}$
Strain energy per domain area	$9.0 \cdot 10^{-3}$	$3.5 \cdot 10^{-3}$	$3.4 \cdot 10^{-3}$

5.3 Physical Size of the Domain

Figures 10(a) to 10(c), show the shapes of fully relaxed tents formed on domains with size 12×12, 25×25 and 50×50 nondimensionalized units. The same number of elements (4096) were used in each computation. Figure 10(d) shows the cross sections of the various surfaces at $y = 0$ for direct comparison.

When the domain size is extremely small, the interfacial energy dominates and the tent is very rounded (Figure 10(a)). Further, no area can be clearly identified as belonging to any variant. However, as the domain size increases, the tent becomes more pyramidal as the sides become flatter with the deformation gradient taking values in the energy wells. The size of the boundary layer in between areas of constant strain does not vary significantly with the domain size; instead the areas of constant strain close to one of the two minima in strain space become larger. Table 2 shows the declining average energy densities for different domain sizes.

5.4 Crystallographic Orientation

The strain energy density (1), and in particular the position of the energy wells, embed information about the crystallography. In the examples above, the crystallography and the physical geometry of the domain were aligned in such a manner as to form a nice tent. Specifically the domain was a square and the preferred interface (ridge) directions coincided with

14

(a) 12×12

(b) 25×25

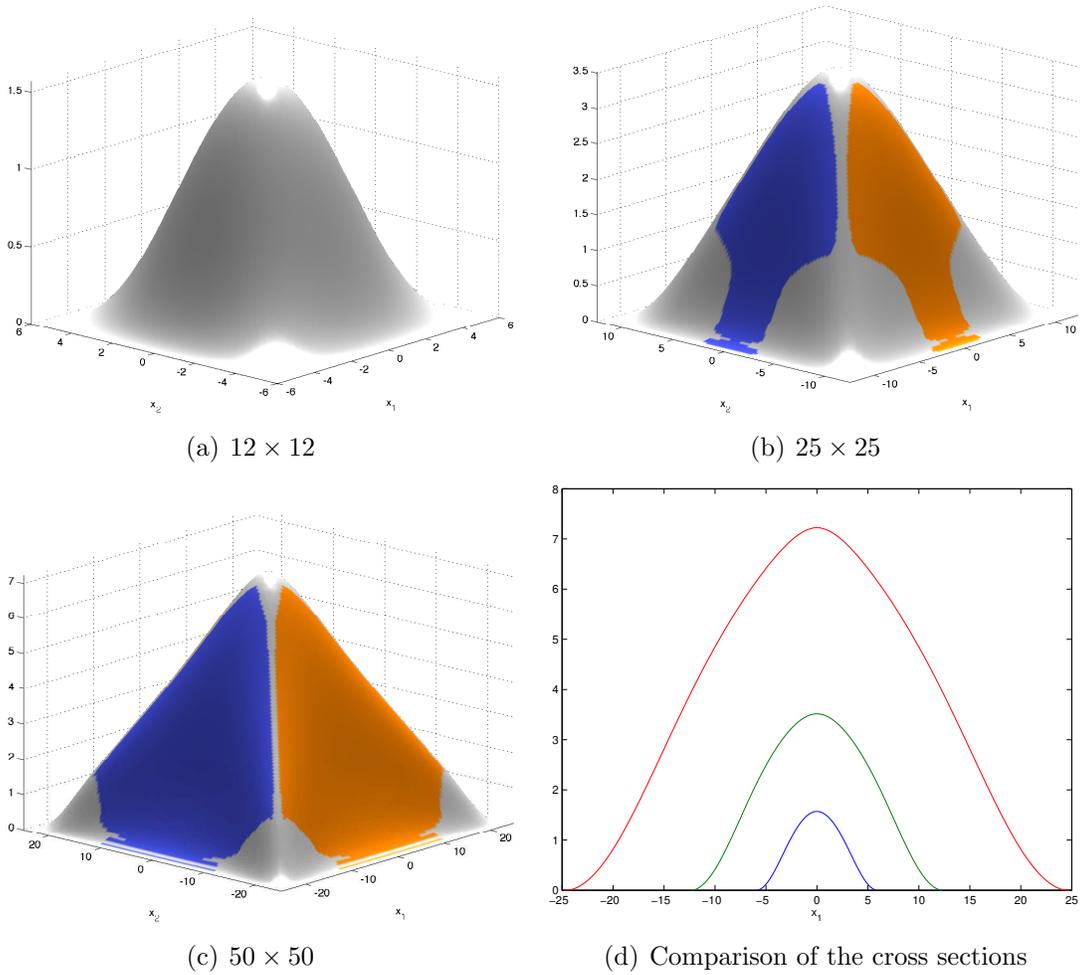(c) 50×50

(d) Comparison of the cross sections

Figure 10: Influence of the physical size of the domain. Color coding as in Figure 7.

Table 3: Comparison of the energies of the tents with various amounts of rotation of the crystallographic axes with respect to the domain.

Rotation	0 degrees	5 degrees	10 degrees	15 degrees
Interfacial Energy	5.2	5.2	5.4	5.8
Strain Energy	8.6	8.7	8.9	9.3

(a) 5 deg

(b) 10 deg

(c) 15 deg

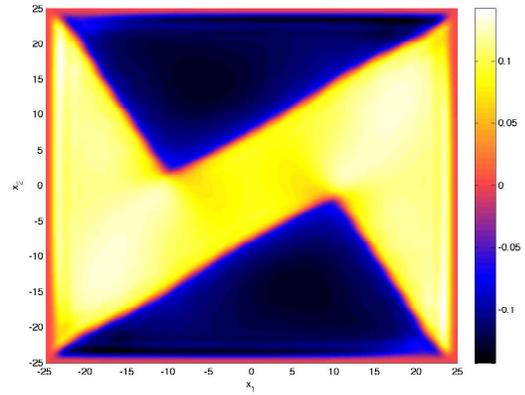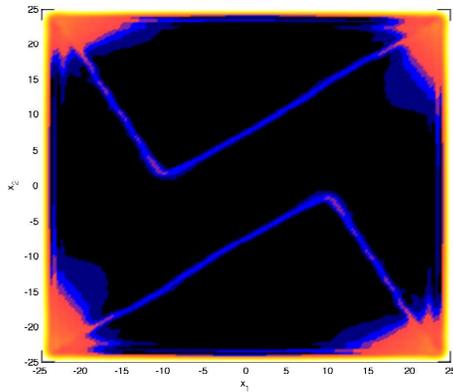(d) Comparison of the cross sections at $x_2 = 0$ and $x_2 = 12.5$
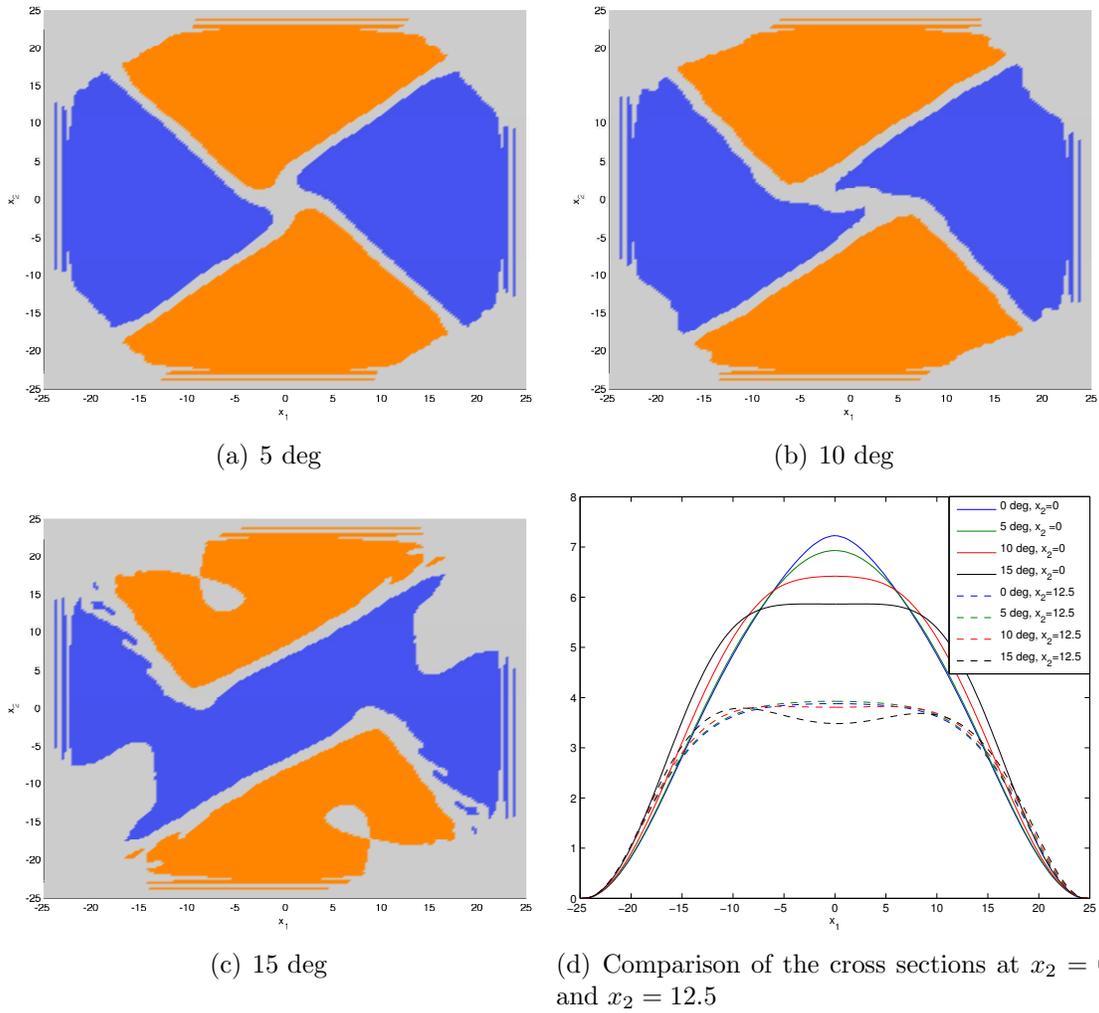
Figure 11: Shapes formed using a crystallographic axis which is rotated with respect to the physical domain. Shown are top views, colors indicate variants as in Figure 7.
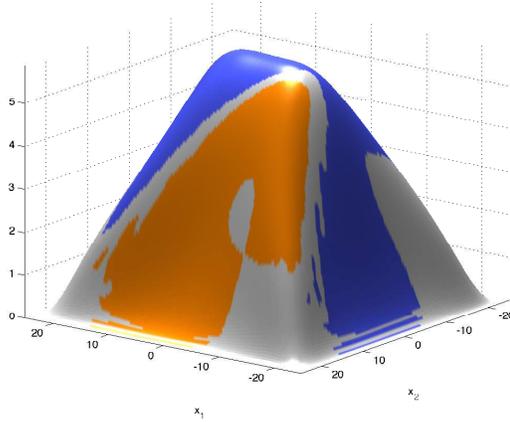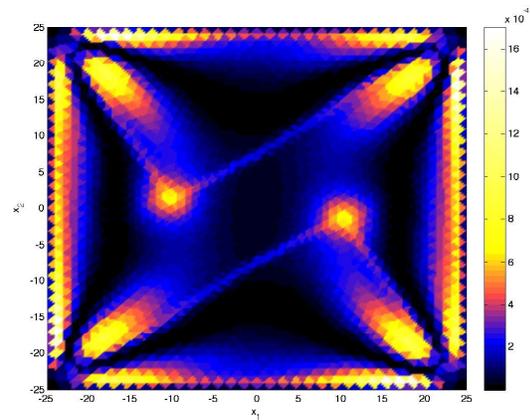
(a) 3D View

(b) $C_{11} - C_{22}$

(c) Strain energy density

(d) Interfacial energy

Figure 12: Detailed view of the tent formed with the crystallographic axes rotated 15 degrees with respect to the domain boundaries.

the diagonals of the domain. In practice, it may prove difficult to provide such an alignment and this section examines the consequences of any misalignment. We keep the orientation of the domain unchanged, but use the rotated energy density (3). The initial conditions and boundary conditions are as before; the domain size is 50×50 nondimensionalized units discretized using 4096 elements.

Figures 11(a) to 11(c) show the equilibriated tents for misalignments of 5°, 10° and 15°. Figure 11(d) shows the sections at $x_2 = 0$ and $x_2 = 12.5$ for various misalignments for comparison. A more detailed analysis of the tent shape formed with the 15 degree misalignment is shown in Figure 12.

It is clear that the shape significantly changes as the misalignment increases. Indeed, the shape becomes less of a square pyramid and more of an elongated mesa with a flat top. Further the height decreases dramatically: the height at the center falls 6%, 14% and 22% with a misalignment of 5°, 10° and 15° respectively relative to a perfectly oriented one. Indeed at 15° the center dips down.

In all these cases, one still has the four sectors of alternating variants. The four ridges that separate the variants follow closely the preferred crystallographic orientation. These, however, are no longer aligned with the squares of the square domain and consequently do not meet at the center of the domain. Instead, the four ridges create a square in the center whose size increases with misalignment. This square is subject to complex deformation as it tries to lie close to one of the energy wells. Table 5.4 confirms this showing increasing energy with misalignment.

These results indicate that for the parameters chosen here, a mismatch of less than 10 degrees in crystallographic orientation and physical domain orientation will somewhat, but not significantly affect the deformed shape. However, at 15 degrees, the outcome is quite different.
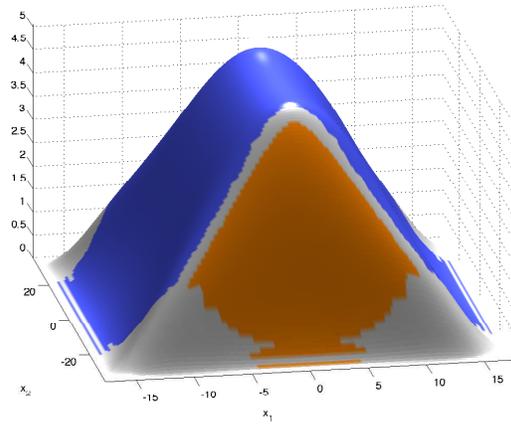
5.5   Rectangular Domain

Figures 13(a) and 13(b) show the equilibriated tent formed on rectangular domains of aspect ratio 0.8 and 0.5, respectively. The crystallographic axis is aligned with the domain. The ridges separating the variants continue to follow their preferred orientation: so the resulting shape is an elongated roof-top. However, the ridge on top is rounded, with the curvature decreasing with increasing aspect ratio. This shape is determined by the competition between interfacial energy along the top ridge and the triple points where the top-ridge meets the two inter-variant ridges. The former scales as aspect ratio and the latter is independent of it. Therefore the interfacial energy dominates for longer domains giving a rounded top while the 'triple point energy' dominates the more square domains giving a less rounded top.

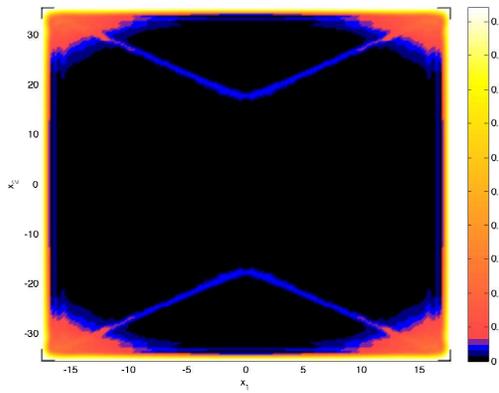# 6   The regular tent revisited

Let us return to the situation described in Section 5.1, and further examine the ridge and the tip. In order to do so, it is convenient to make a coordinate transform that rotates the coordinates by $\pi/4$ so that the ridge forms parallel to the coordinate axes. The energy is
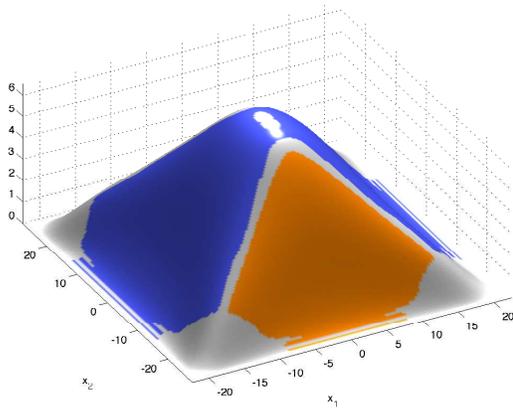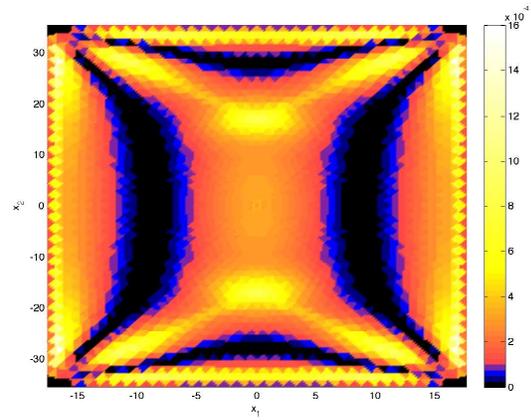
(a) Aspect ratio 0.8

(b) Aspect ratio 0.5

(c) Strain energy density (0.5 aspect ratio)

(d) Interfacial energy density (0.5 aspect ratio)

Figure 13: Tent shapes formed on a rectangular domain.

transformed accordingly and the energy wells are now located at

$$C = \begin{pmatrix} 1 + \frac{1}{2}\xi^2 & \pm\frac{1}{2}\xi^2 \\ \pm\frac{1}{2}\xi^2 & 1 + \frac{1}{2}\xi^2 \end{pmatrix}$$

with C_{12} the non-convex direction. We do not consider any boundary conditions.

Consider a ridge running along $x_2 = $ constant. We anticipate that the deformation gradient to depend only on x_1. So we look for a solution of the form

$$F_{\text{Ridge}} = \begin{pmatrix} \alpha(x_1) & 0 \\ \beta(x_1) & 1 \\ \gamma(x_1) & \frac{1}{\sqrt{2}}\xi \end{pmatrix}. \tag{9}$$

It is easy to verify that this satisfies the compatibility equation

$$\text{curl}\, F_{\text{Ridge}} = 0, \quad \text{or} \quad (F_{\text{Ridge}})_{i\alpha,\beta} = (F_{\text{Ridge}})_{i\beta,\alpha} \text{ where } i = 1...3 \text{ and } \alpha, \beta = 1...2,$$

which ensures that this is indeed a gradient. Plugging this into the equilibrium equation

$$\triangle^2 y + \text{Div}\,\sigma = 0, \tag{10}$$

noting that everything is independent of x_2 and integrating once with respect to x_1 leads to second-order ordinary differential equations for α, β and γ. These equations are

$$\alpha'' = (4a + c)\left(\alpha^2 + \beta^2 + \gamma^2 - 1 - \frac{\xi^2}{2}\right)\alpha,$$

$$\beta'' = (4a + c)\left(\alpha^2 + \beta^2 + \gamma^2 - 1 - \frac{\xi^2}{2}\right)\beta$$

$$+ 2b\,\Phi'\left(2\beta + \sqrt{2}\xi\,\gamma\right)\left(4\left(\beta + \frac{\xi}{\sqrt{2}}\gamma\right)^2 - \xi^4\right)^2$$

$$+ 16b\,\Phi\left(2\beta + \sqrt{2}\xi\,\gamma\right)\left(4\left(\beta + \frac{\xi}{\sqrt{2}}\gamma\right)^2 - \xi^4\right)\left(\beta + \frac{\xi}{\sqrt{2}}\gamma\right),$$

$$\gamma'' = (4a + c)\left(\alpha^2 + \beta^2 + \gamma^2 - 1 - \frac{\xi^2}{2}\right)\gamma$$

$$+ b\xi\sqrt{2}\,\Phi'\left(2\beta + \sqrt{2}\xi\,\gamma\right)\left(4\left(\beta + \frac{\xi}{\sqrt{2}}\gamma\right)^2 - \xi^4\right)^2$$

$$+ 8\sqrt{2}b\xi\,\Phi\left(2\beta + \sqrt{2}\xi\,\gamma\right)\left(4\left(\beta + \frac{\xi}{\sqrt{2}}\gamma\right)^2 - \xi^4\right)\left(\beta + \frac{\xi}{\sqrt{2}}\gamma\right), \tag{11}$$

where the prime denotes differentiation with respect to x_1. If $(4a + c)$ is large, then we may replace the first equation with the constraint

$$\alpha^2 + \beta^2 + \gamma^2 = 1 + \frac{1}{2}\xi^2.$$

This in turn implies that

$$C_{11} = C_{22} = 1 + \frac{1}{2}\xi^2 \tag{12}$$

so that C traverses along the low-energy C_{12} direction across the ridge.

With the change of variables,

$$x = \beta - \frac{\sqrt{2}}{\xi}\gamma, \quad y = \beta + \frac{\xi}{\sqrt{2}}\gamma,$$

these equations simplify to

$$
\begin{aligned}
x'' &= 0 \\
y'' &= b\left(2 + \xi^2\right)\Phi'(2y)\left((2\,y)^2 - \xi^4\right)^2 + 8b\left(2 + \xi^2\right)\Phi(2y)\left((2\,y)^2 - \xi^4\right)y \\
&= b\left(1 + \frac{\xi^2}{2}\right)\frac{\partial}{\partial y}\left(\Phi(2y)\left((2\,y)^2 - \xi^4\right)^2\right).
\end{aligned}
$$

Now assume for the moment that $\Phi = 1$. Recall that we introduced this function to increase the energy barrier between the wells. Then, the second of the equations above reduce to

$$y'' = b\left(1 + \frac{\xi^2}{2}\right)\frac{\partial}{\partial y}\left(\left((2\,y)^2 - \xi^4\right)^2\right)$$

which has a solution

$$y = \frac{\xi^2}{2}\tanh\left(-2\xi^2\sqrt{b\left(2 + \xi^2\right)}\,x_1\right) \tag{13}$$

that smoothly transitions from $-\xi^2/2$ to $\xi^2/2$ over a length-scale of $\left(2\xi^2\sqrt{b\left(2 + \xi^2\right)}\right)^{-1}$. Thus, we have constructed a solution for which F_{Ridge} transitions between

$$\begin{pmatrix} 1 & 0 \\ 0 & 1 \\ \frac{1}{\sqrt{2}}\xi & \frac{1}{\sqrt{2}}\xi \end{pmatrix} \quad \text{and} \quad \begin{pmatrix} 1 & 0 \\ 0 & 1 \\ -\frac{1}{\sqrt{2}}\xi & \frac{1}{\sqrt{2}}\xi \end{pmatrix}.$$

while satisfying the constraint (12). Indeed, a simple calculation shows that $C_{12} = y$, so that C_{12} changes as a hyperbolic tangent as we go across the ridge according to (13). This shows that the width of a typical ridge is of the order $\left(2\xi^2\sqrt{b\left(2 + \xi^2\right)}\right)^{-1}$. Finally, note that the x corresponds to a rotation, and thus its details depend on the exact boundary conditions.

If $\Phi \neq 1$, we are unable to find the profile explicitly, though the above results hold qualitatively. Further, as the barrier increases, the transition region is smaller.

In summary, these calculations show that one can traverse the ridge using the low energy direction as suggested by our computations.

We now turn to the tip, and examine whether can be formed by two crossing ridges. We look for a solution where the deformation gradient is of the form

$$F_{\text{Tip}} = \begin{pmatrix} \alpha_1(x_1) & \alpha_2(x_2) \\ \beta_1(x_1) & \beta_2(x_2) \\ \gamma_1(x_1) & \gamma_2(x_2) \end{pmatrix}. \tag{14}$$

It is easy to verify that while it satisfies the compatibility equation, it can not satisfy the equilibrium equation (10). In other words, the deformation at the tip has to be more complicated than two crossing ridges.

7 Conclusions

The results demonstrate the feasibility of using subdivision surfaces to computationally study thin films undergoing martensitic phase transformations. Specifically, they provide a discretization which is able to naturally and accurately resolve the higher order derivatives, while being simple enough to work with in situations involving non-convex (multi-well) energies.

The work presented here also provides insights into tent-like deformations which are potentially of interest for microactuation. The computations demonstrate that this deformation can be quite complex even in the case where the crystallographic axis is perfectly aligned with the physical domain. In particular, the deformation involves inhomogeneous in-plane stretches in addition to out-of-plane motions and thus can not be described as an antiplane shear motion. The results also show an unexpected breaking of the symmetry at the tip. We provide an analytic studies that confirm the computational results. Second, the numerical calculations show that the overall structure of the tent remains stable for small deviations but begin to deviate substantially beyond 10 degrees of misalignment. Thus we infer that a manufacturing of actuators accurate to about 10 angular degrees should be sufficient to still achieve suitable results. Finally, we show how the shape changes when the released region is a rectangle instead of a square.

An interesting extension to the current simulation would be to allow for adaptive refinement of the discretization. This is especially beneficial in the current situation involving phase transforming materials since we have small regions of large gradients separating large regions of small gradients, and these partitioning is a priori unknown. As demonstrated in [**?**], subdivision surfaces lend themselves to a natural method for adaptive refinement, and its implementation is currently underway.

Appendix A

Our starting point is a one-director Cosserat model of thin films which was shown by Bhattacharya and James [2] to be the rigorous asymptotic (Γ) limit of a three-dimensional theory of martensitic phase transformation. Consider film with lateral extent $\Omega \subset \mathbb{R}^2$ and thickness h in the reference configuration. Let $y : \Omega \to \mathbb{R}^3$ describe the deformation of the mid-surface and $b : \Omega \to \mathbb{R}^3$ be the director that describes the deformation of the thickness. The energy (per unit thickness) of the film is given by

$$\int_\Omega \left\{ \kappa \left(|\nabla^2 y|^2 + 2|\nabla b|^2 \right) + \varphi(\nabla y | b) \right\} dx$$

where the first term (with co-efficient κ) describes the interfacial or exchange energy while the second is the stored energy. φ is the bulk or three-dimensional stored energy density and it is evaluated at the 3×3 matrix constructed as follows: the first two columns are the

partial derivatives of y with respect to the planar co-ordinates while the third is the vector b.

If we impose natural boundary conditions on b, then it is minimized at uniform/constant fields. Thus, the problem above becomes one of minimizing

$$\int_\Omega \left\{ \kappa |\nabla^2 y|^2 + W(\nabla y) \right\} dx$$

over all y subject to appropriate boundary conditions where

$$W(F) = \min_b \varphi(F|b) \ .$$

If W_0 is some characteristic scale of energy density, then

$$\lambda = \sqrt{\frac{\kappa}{W_0}}$$

is a characteristic length-scale. Indeed, if we choose W_0 to be the barrier-height between the wells normalized by the transformation strain, then λ determines the length-scale on which the equilibrium solutions transition from one well to another. Therefore it is natural to non-dimensionalize the problem with λ and W_0:

$$x \mapsto \lambda x, \quad y \mapsto \lambda y, \quad \Omega \mapsto \lambda \Omega, \quad W \mapsto W_0 W \ .$$

We obtain the form of the interfacial and strain energy used in Section 2.

References

[1] Pavel Bělík and Mitchell Luskin. A computational model for the indentation and phase transformation of a martensitic thin film. *J. Mech. Phys. Solids*, 50(9):1789–1815, 2002.

[2] K. Bhattacharya and R. D. James. A theory of thin films of martensitic materials with applications to microactuators. *J. Mech. Phys. Solids*, 47(3):531–576, 1999.

[3] Henning Biermann, Adi Levin, and Denis Zorin. Piecewise smooth subdivision surfaces with normal control. In Kurt Akeley, editor, *Siggraph 2000, Computer Graphics Proceedings*, pages 113–120. ACM Press / ACM SIGGRAPH / Addison Wesley Longman, 2000.

[4] Fehmi Cirak and Michael Ortiz. Fully c^1-conforming subdivision elements for finite deformation thin-shell analysis. *Int. J. Numer. Meth. Engng.*, 51:813–833, 2001.

[5] Fehmi Cirak, Michael Ortiz, and Peter Schröder. Subdivision surfaces: A new paradigm for thin-shell finite-element analysis, March 01 2000.

[6] Eitan Grinspun, Peter Schroder, and Petr Krysl. Natural hierarchical refinement for finite element methods, April 20 2002.

[7] P. Krulevitch, A.P. Lee, P.B. Ramsey, J.C. Trevino, J. Hamilton, and M.A. Northrup. Thin film shape memory alloy microactuators. *J MEMS*, 5(4):270–282, Dec 1996.

[8] Charles Loop. *Generalized B-spline surfaces of arbitrary topological type.* PhD thesis, University of Washington, 1992.

[9] Jos Stam. Evaluation of loop subdivision surfaces, May 21 1998.

[10] D. Zorin and P. Schröder, editors. *Subdivision for Modeling and Animation.* Computer Graphics (SIGGRAPH '99 Course Notes), 1999.